J. Fluid Mech. (2010), *vol.* 656, *pp.* 298–308.
doi:10.1017/S0022112010002740

Lattice Boltzmann method for direct numerical simulation of turbulent flows

S. S. CHIKATAMARLA[1]†, C. E. FROUZAKIS[1], I. V. KARLIN[1,2], A. G. TOMBOULIDES[3] AND K. B. BOULOUCHOS[1]

[1]LAV, Institute of Energy Technology, ETH Zurich, 8092 Zurich, Switzerland
[2]School of Engineering Sciences, University of Southampton, Southampton SO17 1BJ, UK
[3]Department of Mechanical Engineering, University of Western Macedonia, 50100 Kozani, Greece

(Received 29 September 2009; revised 19 April 2010; accepted 10 May 2010; first published online 8 July 2010)

We present three-dimensional direct numerical simulations (DNS) of the Kida vortex flow, a prototypical turbulent flow, using a novel high-order lattice Boltzmann (LB) model. Extensive comparisons of various global and local statistical quantities obtained with an incompressible-flow spectral element solver are reported. It is demonstrated that the LB method is a promising alternative for DNS as it quantitatively captures all the computed statistics of fluid turbulence.

Key words: computational methods, isotropic turbulence, turbulence simulation

1. Introduction

The lattice Boltzmann (LB) method is a relatively new approach to hydrodynamics, with applications ranging from high-Reynolds-number flows to flows at the micron scale, porous media and multi-phase flows (Succi 2001). It solves a fully discrete kinetic equation for the populations $f_i(\boldsymbol{x}, t)$ of fictitious particles designed in such a way as to reproduce the Navier–Stokes equations in the hydrodynamic limit. Populations correspond to discrete velocities $\boldsymbol{c}_i$, $i = 0, \ldots, Q$, which fit into a regular spatial lattice with nodes $\boldsymbol{x}$. This enables a simple and highly efficient 'stream along links and equilibrate at nodes' realization of the LB algorithm.

There are a few recent suggestions to extend the LB method to a higher order of accuracy (Chikatamarla & Karlin 2006, 2009; Philippi *et al.* 2006; Shan, Yuan & Chen 2006). This is due to the fact that current standard LB lattices are not 'sufficiently' Galilean invariant (the feature that LB improved on from its predecessor, the lattice gas model, but failed to resolve completely). Even though the incomplete Galilean invariance of current LB models was recognized earlier (Benzi & Succi 1990; Benzi, Succi & Vergassola 1992; Qian & Orszag 1993), progress was achieved only recently. Insufficient Galilean invariance of standard LB lattices leads to many difficulties, in particular, in applications to high-Reynolds-number hydrodynamics (Hazi & Kavran 2006), multi-phase (Swift *et al.* 1996) and multi-component flows (Arcidiacono *et al.* 2007), compressible flows (Ansumali & Karlin 2005), microflows (Ansumali *et al.* 2007), etc. It is well understood that the current 'standard' LB models are too constrained by the small number of discrete velocities, and lattices with more velocities are required to overcome these limitations. However, early attempts to introduce

† Email address for correspondence: shyam_css@yahoo.com

lattices with more velocities were unsuccessful because of severe numerical instabilities of the resulting LB schemes (McNamara, Garcia & Alder 1995; Qian & Zhou 1998). Discretization of the velocity space using high-order Gauss–Hermite quadrature offers the potential for a systematic derivation of new stable discrete velocity models (Shan & He 1998; Ansumali, Karlin & Öttinger 2003). However, since the roots of Hermite polynomials are irrational, the corresponding discrete velocities do not fit into a regular space-filling lattice. Thus, one of the most important advantages of LB methods, the exact space discretization of particles' advection, is lost with quadrature-based off-lattice models.

Progress was recently achieved by Chikatamarla & Karlin (2006, 2009), where higher-order LB modes were constructed using an entropy function (Karlin, Ferrante & Ottinger 1999). In particular, it was shown that some of the high-order lattices suggested in the past were doomed to fail because of the lack of a supporting entropy function in their construction. The systematic construction of high-order LB models proposed by Chikatamarla & Karlin (2006, 2009) not only recovered the results from the Gauss–Hermite quadrature as a limiting case, but also led to the discovery of new admissible lattices with better properties.

Before these higher-order lattices can be applied to complex fluid dynamics problems, it is important to demonstrate their applicability and stability in the incompressible flow regime. In this paper, we present for the first time three-dimensional turbulent flow simulations using a novel higher-order entropic LB model as well as a standard low-order model. The classical Kida vortex flow at high Reynolds numbers is chosen in order to compare the LB method (in both formulations) with direct numerical simulation (DNS) results obtained using a spectral element incompressible flow solver. The LB method was found to quantitatively reproduce the DNS results, and also lead to significant savings in computational time compared to the spectral element solver. We also demonstrate that the new higher-order LB model is superior to the standard LB method in terms of Galilean invariance and stability at high-Reynolds-number flows.

The outline of the paper is as follows. In § 2, we review the multi-speed LB models, along with a numerical demonstration of its Galilean invariance. In § 3, we present three-dimensional simulations of the Kida vortex flow using a spectral element solver and the LB method. Detailed comparison of the statistics of various physical quantities computed from simulation results in terms as well as quantitative run times for both methods are presented.

2. Galilean invariant multi-speed lattice Boltzmann model

In this section, the derivation of the multi-speed LB models (Chikatamarla & Karlin 2006, 2009) is reviewed briefly. The construction proceeds in three steps: (i) derivation of admissible lattices in one spatial dimension. In this step, one-dimensional velocity sets V with Q integer-valued discrete velocities are found from a condition that the higher-order moments of the equilibrium (obtained by minimizing the entropy function) are Galilean invariant. From this requirement, the reference temperature T_0 for each admissible set V can be derived. The reference temperature, in particular, is equal to the square speed of sound ($T_0 = c_s^2$) in the expression for the equilibrium pressure $P^E = \rho c_s^2 + \rho u^2$. (ii) The one-dimensional velocity sets found in step (i) are extended into three dimensions using a tensor-product expansion. The tensor-product lattice can be naturally expressed in terms of groups of velocities with the same magnitude (energy shells). (iii) The tensor-product lattice is reduced by systematically discarding some of the energy shells (pruning).

ϵ	V_ϵ	Q_ϵ	$W_\epsilon = W_{i^2+j^2+k^2}$
0	$\{(0,0,0)\}$	1	$2(5045-1507\sqrt{10})/2025$
1	$\{(\pm1,0,0),(0,\pm1,0),(0,0,\pm1)\}$	6	$377/(5\sqrt{10})-(91/40)$
2	$\{(\pm1,\pm1,0),(\pm1,0,\pm1),(0,\pm1,\pm1)\}$	12	$(55-17\sqrt{10})/50$
3	$\{(\pm1,\pm1,\pm1)\}$	8	$(233\sqrt{10}-730)/1600$
9	$\{(\pm3,0,0),(0,\pm3,0),(0,0,\pm3)\}$	6	$(295-92\sqrt{10})/16\,200$
27	$\{(\pm3,\pm3,\pm3)\}$	8	$(130-41\sqrt{10})/129\,600$

TABLE 1. The D3Q41 lattice. First column: energy shells $\epsilon = i^2+j^2+k^2$ in increasing order; second column: velocity sets V_ϵ constituting energy shells ϵ; third column: number of velocities Q_ϵ in each energy shell; fourth column: weights W_ϵ corresponding to each discrete velocity in a given energy shell ϵ. The D3Q41 velocity set is a joint of all the sets V_ϵ displayed in the second column.

In this paper, we consider the velocity set $V=\{-3,-1,0,1,3\}$ ($Q=5$), for which the reference temperature is

$$T_0 = 1-\sqrt{2/5}. \tag{2.1}$$

The three-dimensional extension of this set, formed by the tensor product of V, consists of $Q=125$ discrete velocities $\boldsymbol{c}=(i,j,k)$, $i,j,k\in\{-1,-3,0,1,3\}$, which can be grouped into ten energy shells, each energy shell V_ϵ being a subset of discrete velocities with the same energy $\epsilon = i^2+j^2+k^2$. In the pruning procedure, we consider subsets S of the 10 energy shells, and require that an entropy function H of functional form

$$H = \sum_{\epsilon\in S}\sum_{(i,j,k)\in V_\epsilon} f_{(i,j,k)}\ln\left(\frac{f_{(i,j,k)}}{W_\epsilon}\right), \tag{2.2}$$

exists such that its minimizer under fixed density and momentum renders the higher-order equilibrium moments required to recover the Navier–Stokes equations Galilean invariant. This amounts to finding the weights $W_\epsilon>0$ corresponding to each of the retained energy shells in function (2.2). In this paper, the D3Q41 lattice is considered. The retained energy shells together with the corresponding weights are specified in table 1.

Once the entropy function H is defined, the equilibrium is obtained by computing its minimum under fixed density and momentum. The minimization problem can be efficiently solved by employing the product form of equilibrium (Chikatamarla, Ansumali & Karlin 2006). The equilibrium populations are represented as

$$f^E_{(i,j,k)} = \rho W_\epsilon A B_x^i B_y^j B_z^k, \tag{2.3}$$

where Lagrange multipliers A and B_α have the following series expansion to order $O(u^8)$:

$$\begin{aligned} A = 1 &- \frac{u^2}{2T_0}+\frac{u^4}{8T_0^2}-\frac{(3-2T_0(5-3T_0))u^6}{48T_0^5}+\frac{(5(T_0-2)T_0+3)}{16T_0^5}X \\ &-\frac{(6-T_0(6T_0(7T_0-16)+47))u^8}{384T_0^7}-\frac{(T_0(T_0(18T_0-43)+22)-3)}{48T_0^7}u^2X \\ &+\frac{(7T_0(T_0+1)-3)}{96T_0^7}\left(u_x^4u_y^4+u_y^4u_z^4+u_x^4u_z^4\right)+\frac{(2(14T_0(5T_0-1)-3))}{96T_0^7}u_x^2u_y^2u_z^2u^2, \end{aligned} \tag{2.4}$$

$$X = \left(u_x^2 + u_y^2\right)\left(u_x^2 + u_z^2\right)\left(u_y^2 + u_z^2\right);$$

$$B_\alpha = \frac{u_\alpha}{T_0} + \frac{u_\alpha^2}{2T_0^2} + \frac{u_\alpha^3}{6T_0^3} + \frac{u_\alpha^4}{24T_0^4} + \frac{(3(T_0-2)T_0+2)u_\alpha^5}{24T_0^5} + \frac{(18(T_0-2)T_0+11)u_\alpha^6}{144T_0^6} + \frac{(8-3T_0(T_0(3T_0-11)+11))u_\alpha^7}{144T_0^7} + \frac{(35-24T_0(3(T_0-3)T_0+7))u_\alpha^8}{1152T_0^8} + B'_\alpha, \quad (2.5)$$

$$B'_\alpha = \frac{(3T_0-1)}{48T_0^6}\left(u_\alpha + \frac{u_\alpha^2}{T_0}\right)\left[(T_0-3)\left(u_\beta^4 + u_\gamma^4\right)u_\alpha^2 + (T_0-9)u_\beta^2 u_\gamma^2\left(u_\alpha^2 + u^2\right)\right], \ \beta \neq \gamma \neq \alpha. \quad (2.6)$$

The product-form equilibrium (2.3) is particularly efficient for simulations at low Mach numbers which is the objective of this paper. Once the equilibrium is defined, we use the lattice Bhatnagar–Gross–Krook (LBGK) scheme

$$f_{(i,j,k)}(\boldsymbol{x}+\boldsymbol{c}, t+1) - f_{(i,j,k)}(\boldsymbol{x}, t) = \frac{2}{2\tau+1}\left(f^E_{(i,j,k)}(\boldsymbol{x}, t) - f_{(i,j,k)}(\boldsymbol{x}, t)\right). \quad (2.7)$$

In the low-Mach-number limit, the LB equation (2.7) recovers the Navier–Stokes equations at the reference temperature T_0, with kinematic viscosity $\nu = \tau T_0$. It is instructive to compare the accuracy of the Navier–Stokes equations recovered by the present D3Q41 LB model with the accuracy of the standard LB model for incompressible flow simulations. We note here that the standard three-dimensional D3Q27 LB is generated as the tensor product of the one-dimensional velocity set $V = \{-1, 0, 1\}$ ($Q = 3$, corresponding to the reference temperature $T_0 = 1/3$), followed by pruning to derive the commonly used D3Q19 and D3Q15 models.

In order to make a comparison, the Lagrange multipliers (2.4), (2.5) and (2.6) are substituted into (2.3), the resulting equilibrium is expanded into powers of u_α to order u^3, and the equilibrium pressure tensor $P^E_{\alpha\beta} = \sum_i f_i^E c_{i\alpha} c_{i\beta}$ and third-order moment tensors $Q^E_{\alpha\beta\gamma} = \sum_i f_i^E c_{i\alpha} c_{i\beta} c_{i\gamma}$, which are required to recover isothermal Navier–Stokes equations by the LBGK model (2.7) are computed. The D3Q41 model recovers the Galilean invariant expressions:

$$\left.\begin{aligned} P^E_{\alpha\beta} &= \rho T_0 \delta_{\alpha\beta} + \rho u_\alpha u_\beta, \\ Q^E_{\alpha\beta\gamma} &= \rho T_0 (u_\alpha \delta_{\beta\gamma} + u_\beta \delta_{\alpha\gamma} + u_\gamma \delta_{\alpha\beta}) + \rho u_\alpha u_\beta u_\gamma. \end{aligned}\right\} \quad (2.8)$$

On the contrary, the third-order moment $Q^E_{\alpha\beta\gamma}$ of the standard D3Q27, D3Q19 and D3Q15 LB models is recovered only up to $O(u)$: $Q^E_{\alpha\beta\gamma} = \rho T_0(u_\alpha \delta_{\beta\gamma} + u_\beta \delta_{\alpha\gamma} + u_\gamma \delta_{\alpha\beta}) + O(u^3)$, where the deviation terms $O(u^3)$ are present in all three models.

In the standard LB models, these deviations result in a spurious dependence of the kinematic viscosity on the fluid velocity, thus limiting their range of applicability (Benzi & Succi 1990; Benzi *et al.* 1992; Qian & Orszag 1993; Succi 2001). Such a spurious dependence is not present in the D3Q41 model. This can be demonstrated by a simulation of the decay of a shear wave which we present first. A periodic box of fluid is initialized with equilibrium distributions computed at constant density and a velocity given by

$$\boldsymbol{u} = \boldsymbol{u}_0 + a_0 \sin(2\pi z/N_z)\, \boldsymbol{e}_x, \quad (2.9)$$

where $\boldsymbol{u}_0 = (0, u_{0y}, u_{0z})$ is the reference frame velocity and a_0 is the small initial amplitude of the shear in the direction $\boldsymbol{e}_x$. A simulation domain of $N_z = 100$ nodes in the z direction and $N_x = N_y = 5$ nodes in the x and y directions was chosen with periodic boundary conditions on all three sides. Two LBGK models of the form (2.7)

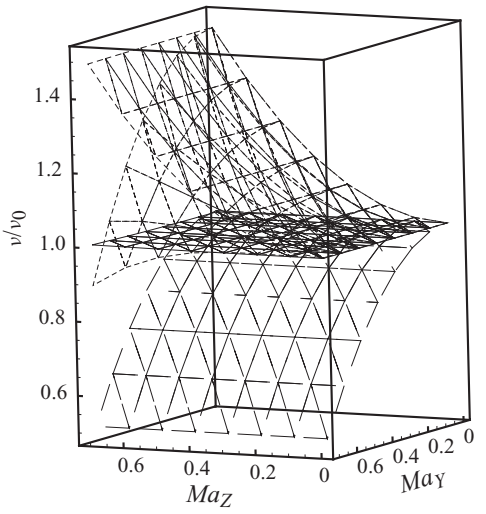

FIGURE 1. Decay of the shear wave in a moving reference frame. Reduced kinematic viscosity ν/ν_0, where ν_0 corresponds to $\boldsymbol{u}_0 = 0$, as a function of the Y and Z Mach numbers is measured for the present D3Q41 (solid) and the standard D3Q15 LB models. Anisotropic and spurious dependence of viscosity of the order of the equilibrium distributions is seen for the D3Q15 model (the dashed surfaces, in the increasing order of dash-size, represent D3Q15 simulations using second-, third- and fourth-order equilibrium distributions).

were studied at various frame velocities: the standard D3Q15 model and the present D3Q41 model with the equilibrium obtained by expanding the product form (2.3)–(2.6) to third order in the velocity $\boldsymbol{u}$. This is needed in order to keep the conservation laws under control at larger values of the velocity.

Figure 1 shows the influence of the Y and Z Mach numbers, $Ma_Z = u_{0z}/\sqrt{T_0}$ and $Ma_Y = u_{0y}/\sqrt{T_0}$, respectively, on the measured kinematic viscosity. An LB model is termed complete Galilean invariant if the measured viscosity is independent of the frame velocity (Qian & Zhou 1998). It can be clearly seen that while the D3Q41 LB model is Galilean invariant, the viscosity of the standard D3Q15 LB model depends strongly on the frame velocity. We now proceed with the turbulent flow simulations using the D3Q41 LB model.

3. Direct numerical simulation of turbulent vortex flow

A detailed comparison of the accuracy and efficiency of LB methods for simulating fluid turbulence is the main objective of this paper. The Taylor–Green and the Kida vortex flows are benchmark flows where simple initial conditions evolve in time to a turbulent flow. Both flows have been analysed extensively using DNS; the former by Orszag (1983) and Brachet (1991), and the latter by Kida (1985), Kida & Murakami (1987), Boratav & Pelz (1994), Keating *et al.* (2007) and others. We investigate here in detail the Kida vortex flow using the LB method and an incompressible flow solver based on the spectral element method (SEM).

The Kida vortex flow is initialized by the velocity field

$$\left.\begin{aligned} u_x(x, y, z, 0) &= U_0 \sin x(\cos 3y \cos z - \cos y \cos 3z), \\ u_y(x, y, z, 0) &= U_0 \sin y(\cos 3z \cos x - \cos z \cos 3x), \\ u_z(x, y, z, 0) &= U_0 \sin z(\cos 3x \cos y - \cos x \cos 3y), \end{aligned}\right\} \tag{3.1}$$

where $x \in [0, 2\pi]$, and periodic boundary conditions are imposed in all directions. A detailed summary of this flow, including its symmetries are discussed by Kida (1985). Some of the symmetries that are present in this flow are 2π periodicity, bilateral symmetry through planes $n\pi$, $n = 0, +1, +2, \ldots$, a $\pi/2$ rotational symmetry around the axis $(\pi/2, \pi/2)$ and permutation symmetry of the velocity components, $u_x(x, y, z) = u_y(y, z, x) = u_z(z, x, y)$. Using these symmetries (i.e. simulating only the independent Fourier modes), the memory and computational requirements can be reduced when using Fourier spectral methods. Such optimizations were used to produce high-resolution DNS for this flow (see e.g. Boratav & Pelz 1994). These optimizations are characteristic to this flow set-up, and cannot be exploited by conventional techniques like finite difference, or even the LB method and SEM; all simulations presented here do not take advantage of these symmetries.

The Reynolds number is defined based on the initial condition, $Re = LU_0/\nu$, where L is the domain size and ν the kinematic viscosity. The kinetic energy, Ke, initially stays relatively constant, reflecting the inviscid nature of the flow in the early stages. On the other hand, the enstrophy Ω initially increases almost exponentially, reaches a maximum value which depends on the Re, and then decays. As the Reynolds number increases, this early-time behaviour of almost constant Ke and steep increase in Ω intensifies. Since this flow resembles a fully developed turbulent flow, especially after the peak of enstrophy, we investigate in detail data collected from this regime.

For comparison, the incompressible Navier–Stokes equations were solved using and incompressible flow solver based on the SEM (Patera 1984). The temporal discretization is based on a second-order mixed explicit/implicit operator splitting formulation (Karniadakis, Israeli & Orszag 1991; Tomboulides, Israeli & Karniadakis 1989). Various spatial discretizations were employed with 32 spectral elements in each direction and the number of collocation points ranging from 8 to 12 in each direction in the interior of each element, corresponding to an overall grid resolution of up to 353^3 (after removing redundant points). An MPI-based parallel spectral element code, nek5000, with very good scalability was used (`https://nek5000.mcs.anl.gov/index.php/Main_Page`). Simulations were performed on 32 or 64 AMD 2.5 GHz processors.

The simulations were performed for $Re = 4000$ in a domain of size $L = 1$, velocity $U_0 = 1$ and grid resolution of 353^3 for the SEM. In the LB simulation, the same Re with velocity $U_0 = 0.05$ and a grid resolution of 352^3 ($L = 352$) was employed. Note that the SEM grid is a non-uniform grid within each element, while in the LB method a uniform Cartesian mesh is chosen to make the advection step of the LBGK equation (2.7) exact.

The LB simulations using the new D3Q41 model as well as the standard D3Q15 model were performed using a similar code structure and the equilibrium expressed in the product form. Due to the linear scaling of the product form (cf. Chikatamarla *et al.* 2006), the D3Q41 simulations were only about 2.3 times slower compared to the D3Q15 simulations. Since the initial conditions for the flow are known only in terms of low-order moments (density and velocity), the higher-order moments for the LB simulations were obtained by the iterative process described in Mei *et al.* (2006). Each simulation produces information regarding the velocity and pressure fields at more than 40 million grid points at each time step. Snapshots of the velocity field at selected time instances were stored and post-processed in order to compare various statistics of the turbulent flow. The velocity fields obtained from SEM (after spectrally interpolating to an equidistant grid) and LB method were subject to the same post-processing. The following quantities were computed.

Time (t)	Ke (DNS)	Ke (D3Q15)	Ke (D3Q41)	Ω (DNS)	Ω (D3Q15)	Ω (D3Q41)
0.197	0.601	0.601 (0.0 %)	0.601 (0.0 %)	397.28	399.63 (0.6 %)	400.20 (0.7 %)
0.345	0.528	0.526 (0.4 %)	0.525 (0.6 %)	699.17	675.70 (3.4 %)	667.75 (4.7 %)
0.509	0.396	0.404 (2.0 %)	0.399 (0.8 %)	719.88	698.78 (2.9 %)	685.10 (5.0 %)
0.708	0.280	0.284 (1.4 %)	0.283 (1.0 %)	493.06	481.75 (2.3 %)	478.45 (3.0 %)

TABLE 2. Enstrophy and kinetic energy at various time instants ($Re = 4000$). Percentage deviation between LB and DNS results are indicated in parenthesis.

Skewness	DNS	D3Q15	D3Q41
S_3	0.459	0.417	0.403
S_4	5.069	5.090	4.915
S_5	6.762	6.314	5.770
S_6	51.406	51.205	47.303

TABLE 3. Comparison of the skewness factors for SEM, 15 and 41 velocity lattices, at time $t = 0.708$ ($Re = 4000$).

(i) Enstrophy and kinetic energy: the enstrophy $\Omega = 1/(2V)\int \omega^2 \,\mathrm{d}V$, where $\omega = \nabla \times u$ is the vorticity, and kinetic energy $Ke = 1/(2V)\int u^2 \,\mathrm{d}V$, are two important global quantities characterizing the flow and its history. The kinetic energy and the enstrophy at various times is given in table 2. Overall, the deviation between the SEM and LB method does not exceed 2 % in Ke and 3.4 % in Ω for the D3Q15, and 1.0 % in Ke and 5.0 % in Ω for the D3Q41 models, respectively.

(ii) Skewness factor: the longitudinal skewness function localized at $r = 0$ is defined as

$$S_n = (-1)^n \left\langle (\partial u_x/\partial x)^n \right\rangle \left\langle (\partial u_x/\partial x)^2 \right\rangle^{-n/2}, \tag{3.2}$$

where, $r = 1, 2, \ldots N$. The angular brackets $\langle \phi(x, y, z) \rangle$ denote average of the quantity α over the domain. The comparison of the skewness factor for both DNS and LB method at time $t = 0.708$ is reported in table 3.

So far, averaged and global quantities have been compared; however, to gain better understanding of the quality of the results from the LB simulations obtained further comparisons are needed using local quantities.

(iii) Energy spectrum: initially, all the energy is contained in the smallest wavenumbers (the largest scales) of the system. As the flow evolves, the large initial vortex undergoes vortex stretching and then breaks up into smaller vortices. During this process, energy is transferred to higher wavenumbers through the action of the nonlinear terms of the Navier–Stokes equations. The distribution of the energy is most conveniently seen in a spherically averaged (pure shear) energy spectrum, which is defined here by a band average as

$$KE(k) = \sum_{k \leqslant k' < k+1} |\hat{u}(k')|^2, \quad k = 0, 1, 2, \ldots, \tag{3.3}$$

where $\hat{u}_\alpha(k_x, k_y, k_z)$ is the three-dimensional discrete Fourier transform of the velocity field $u_\alpha(x, y, z)$. The spherical wavenumber k is defined as $k^2 = k_x^2 + k_y^2 + k_z^2$, and $|\hat{u}(k)|^2 = |\hat{u}_x(k)|^2 + |\hat{u}_y(k)|^2 + |\hat{u}_z(k)|^2$ is collected into the corresponding wavenumber k. The same post-processing routine was used for both methods. Figure 2 compares the energy spectrum for the SEM and LB method at $t = 0.708$. Excellent agreement

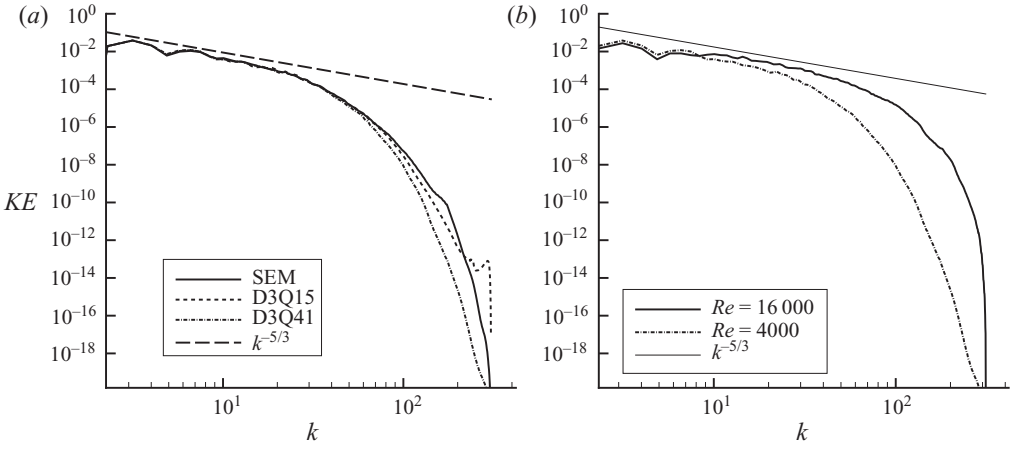

FIGURE 2. (*a*) Pure shear energy spectrum at $t = 0.708$ ($Re = 4000$). A line with slope $-5/3$ shows the scaling of low-wavenumber modes. (*b*) Pure shear energy spectrum for the D3Q41 LB simulation at $Re = 16\,000$ and a grid size of 360^3 (for comparison the energy spectrum for $Re = 4000$ is plotted with arbitrary scaling).

is observed between the two methods for $k \lesssim 90$ (or scales with $KE \gtrsim 10^{-6}$). Although the flow is turbulent, the Reynolds number, $Re = 4000$, is relatively low to see an extended inertial range.

(iv) Structure functions: the longitudinal structure function of order n is a local quantity defined as

$$B_{ll}^{n}(r) = \langle [u_x(x, y, z) - u_x(x + r, y, z)]^n \rangle . \tag{3.4}$$

According to Kolmogorov (1941), the structure functions for isotropic turbulence are linear on logarithmic plots. Although the Reynolds number in the present simulation is relatively low to see an extended inertial range, the structure function is nevertheless a good measure to probe different numerical methods. Figure 3(*a*) shows the very good agreement of the second-order structure function from the SEM and LB simulations at $t = 0.708$. Very good agreement between the two methods over the entire range of r was also observed for higher-order structure functions.

(v) Two-point velocity correlations: another relevant quantity that can be used to assess different numerical techniques is the correlation of the velocity field. The longitudinal and transversal velocity correlation functions are defined here as

$$\rho_{11}(r) = \frac{\langle u_x(x, y, z) u_x(x + r, y, z) \rangle}{\langle u_x(x, y, z) u_x(x, y, z) \rangle}, \quad \rho_{22,33}(r) = \frac{\langle u_{y,z}(x, y, z) u_{y,z}(x + r, y, z) \rangle}{\langle u_{y,z}(x, y, z) u_{y,z}(x, y, z) \rangle}. \tag{3.5}$$

The comparison at $t = 0.708$ is shown in figure 3(*b*). As expected, both components of the transversal correlation functions (ρ_{22} and ρ_{33}) are very similar and good agreement is observed between the two methods, for all three components of the correlation function. The symmetry of the flow, i.e. the presence of two-similar vortex structures within the domain with 2π periodicity can also be inferred from this figure.

(vi) Summary of comparison with DNS: Before we compare the run time for both simulations, it must be mentioned that for the case under study the two methods used, SEM and LB method, are not optimal. The Kida vortex flow has a number of symmetries which can only be exploited by a global Fourier method. Our interest here is not to use the optimal technique to solve the Kida vortex flow, rather, we

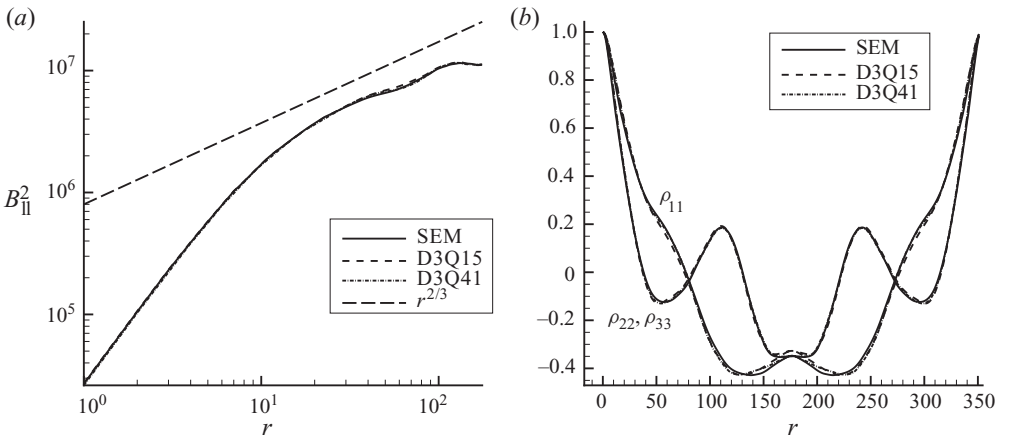

FIGURE 3. (*a*) Comparison of second-order structure function. Straight dash line indicates the Kolmogorov asymptotics for isotropic turbulence. (*b*) Comparison of the two-point longitudinal and transversal correlation functions.

wish to compare the LB simulations with a conventional high-order DNS solver for a benchmark turbulent flow.

The computational times (wall clock time) for the above simulations at $Re = 4000$, from $t = 0$–0.708, on the same 64 processor cluster, were roughly 20 h for the SPM (effective grid of 353^3) and around 0.5 and 1.25 h for the D3Q15 and D3Q41 LB models, respectively (grid 352^3). Although reasonable choices are made for parameters, further code and parameter optimizations may still be possible for both LB method and SEM. These run times indicate that the LB methods are an order of magnitude faster compared to SEM for this problem. However, it should be noted that although the D3Q41 method is defined as a high-order method, the term 'high' refers to its recovery of higher-order moments, relevant to Galilean invariance. On the other hand, SEM, being a high-order method in terms of spatial convergence rate, couples 8–12 points in each spatial direction (corresponding to the polynomial orders used in this work). It is well known that using the same total number of points with high-order methods results in significantly higher accuracy.

Finally, in the above simulations, a moderate Reynolds number was chosen in order to compare the three solutions (SEM, the standard D3Q15 and the new D3Q41 LB models). The two LB models show similar behaviour which is not surprising since the absolute value of the velocity is small compared to the LB speed of sound, and thus deviation due to incomplete Galilean invariance of the D3Q15 is negligible. Small deviations were seen in sensitive quantities like skewness factor. Excellent comparison was obtained for all other quantities such as enstrophy, kinetic energy, energy spectrum, structure functions and two-point velocity correlations. On the other hand, we observed that the multi-speed D3Q41 is more robust in terms of numerical stability when the Reynolds number was increased, thus allowing simulations at higher Reynolds numbers on a given grid size. For example, with a grid of 352^3 lattice points, the simulation on D3Q15 lattice becomes unstable slightly over $Re = 12\,000$, while the simulation on the D3Q41 lattice remains stable at least till $Re = 23\,000$. Figure 2 shows the energy spectrum for the $Re = 16\,000$ on the D3Q41 lattice with a larger inertial range as compared to the $Re = 4000$ case. It is also worth mentioning here that, for entropic LB models, stability can be further enhanced by employing the

entropic time-stepping process (Karlin *et al.* 1999; Keating *et al.* 2007), instead of the LBGK time stepping (defined in (2.7)) used in the current simulations.

These detailed and quantitative comparisons show that the LB method can be considered as an alternative to DNS of high-Reynolds-number flows. We have also demonstrated, for the first time, that higher-order entropic LB models are computationally efficient and more stable and thus should be considered as a basis for further development of LB methods to other areas of fluid dynamics like compressible flows, multi-phase flows, etc.

The authors would like to thank S. Ansumali, P. Fischer, S. Kerkemeier, S. A. Orszag, X. Shan and S. Succi for useful discussions. This work was partially supported by CCEM-CH (I.V.K.).

REFERENCES

Ansumali, S. & Karlin, I. V. 2005 Consistent lattice Boltzmann method. *Phys. Rev. Lett.* **95**, 260605.

Ansumali, S., Karlin, I. V., Arcidiacono, S., Abbas, A. & Prasianakis, N. I. 2007 Hydrodynamics beyond Navier–Stokes: exact solution to the lattice Boltzmann hierarchy. *Phys. Rev. Lett.* **98**, 124502.

Ansumali, S., Karlin, I. V. & Öttinger, H. C. 2003 Minimal entropic kinetic models for simulating hydrodynamics. *Europhys. Lett.* **63**, 798–804.

Arcidiacono, S., Karlin, I. V., Mantzaras, J. & Frouzakis, C. E. 2007 Lattice Boltzmann model for the simulation of multi-component mixtures. *Phys. Rev.* E **76**, 046703.

Benzi, R. & Succi, S. 1990 Two-dimensional turbulence with the lattice Boltzmann equation. *J. Phys.* A **23** (1), L1–L5.

Benzi, R., Succi, S. & Vergassola, M. 1992 The lattice Boltzmann equation: theory and applications. *Phys. Rep.* **222**, 145–197.

Boratav, O. N. & Pelz, R. B. 1994 Direct numerical simulation of transition to turbulence from a high-symmetry initial condition. *Phys. Fluids* **6**, 2757.

Brachet, M. E. 1991 Direct simulation of three-dimensional turbulence in the Taylor–Green vortex. *Fluid Dyn. Res.* **8**, 1.

Chikatamarla, S. S., Ansumali, S. & Karlin, I. V. 2006 Entropic lattice Boltzmann models for hydrodynamic in three dimensions. *Phys. Rev. Lett.* **97**, 010201.

Chikatamarla, S. S. & Karlin, I. V. 2006 Entropic and Galilean invariance of lattice Boltzmann theories. *Phys. Rev. Lett.* **97**, 090601.

Chikatamarla, S. S. & Karlin, I. V. 2009 Lattices for the lattice Boltzmann method. *Phys. Rev.* E. **79**, 046701.

Hazi, G. & Kavran, P. 2006 On the cubic velocity deviations in lattice Boltzmann methods. *J. Phys.* A*: Math. Gen.* **39** (12), 3127–3136.

Karlin, I. V., Ferrante, A. & Ottinger, H. C. 1999 Perfect entropy functions of the lattice Boltzmann method. *Europhys. Lett.* **47**, 182–188.

Karniadakis, G. E., Israeli, M. & Orszag, S. A. 1991 High-order splitting methods for the incompressible Navier–Stokes equations. *J. Comput. Phys.* **97**, 414.

Keating, B., Vahala, G., Yepez, J., Soe, M. & Vahala, L. 2007 Entropic lattice Boltzmann representations required to recover Navier–Stokes flows. *Phys. Rev.* E **75**, 036712.

Kida, S. 1985 Three-dimensional periodic flows with high-symmetry. *J. Phys. Soc. Japan* **54**, 2132.

Kida, S. & Murakami, Y. 1987 Kolmogorov similarity in freely decaying turbulence. *Phys. Fluids* **30**, 2030.

Kolmogorov, A. N. 1941 The local structure of turbulence in an incompressible fluid with very large Reynolds number. *C. R. Acad. Sci.* **30**, 301.

McNamara, G. R., Garcia, A. L. & Alder, B. J. 1995 Stabilization of thermal Lattice Boltzmann models. *J. Stat. Phys.* **81**, 395–408.

Mei, R., Luo, L. S., Lallemand, P. & d'Humieres, D. 2006 Consistent initial conditions for lattice Boltzmann simulations. *Comput. Fluids* **35**, 855–862.

Orszag, S. A. 1983 Numerical simulation of the Taylor–Green vortex. *Proc. Symp. Comput. Method. Appl. Sci. Engng* **50**, 50.

Patera, A. T. 1984 A spectral element method for fluid dynamics: laminar flow in a channel expansion. *J. Comput. Phys.* **54**, 468–488.

Philippi, P. C., Hegele Jr, L. A., Dos Santos, L. O. & Surmas, R. 2006 From the continuous to the lattice Boltzmann equation: the discretization problem and thermal models. *Phys. Rev.* E **73** (5 Pt 2), 056702.

Qian, Y. H. & Orszag, S. A. 1993 Lattice BGK models for the Navier–Stokes equation: nonlinear deviation in compressible regimes. *Europhys. Lett.* **21**, 255–259.

Qian, Y.-H. & Zhou, Y. 1998 Complete Galilean-invariant lattice BGK models for the Navier–Stokes equation. *Europhys. Lett.* **42** (4), 359–364.

Shan, X. W. & He, X. 1998 Discretization of the velocity space in the solution of the Boltzmann equation. *Phys. Rev. Lett.* **80**, 65.

Shan, X. W., Yuan, X. & Chen, H. 2006 Kinetic theory representation of hydrodynamics: a way beyond the Navier–Stokes equation. *J. Fluid Mech.* **550**, 413–441.

Succi, S. 2001 *The Lattice Boltzmann Equation for Fluid Dynamics and Beyond*. Oxford University Press.

Swift, M. R., Orlandini, E., Osborn, W. R. & Yeomans, J. M. 1996 Lattice Boltzmann simulations of liquid-gas and binary fluid systems. *Phys. Rev.* E **54**, 5041.

Tomboulides, A. G., Israeli, M. & Karniadakis, G. E. 1989 Efficient removal of boundary-divergence errors in time-splitting methods. *J. Sci. Comput.* **4**, 291.